Interface formation for a ferromagnetic/antiferromagnetic bilayer system studied by scanning tunneling microscopy and first-principles theory

Andrada-Oana Mandru, Jeongihm Pak, and Arthur R. Smith*
Nanoscale and Quantum Phenomena Institute, Department of Physics and Astronomy, Ohio University, Athens, Ohio 45701, USA

Jonathan Guerrero-Sanchez
Benemérita Universidad Autónoma de Puebla, Instituto de Física "Ing Luis Rivera Terrazas", Apartado Postal J-48, Puebla 72570, México

Noboru Takeuchi
Centro de Nanociencias y Nanotecnologia, Universidad Nacional Autónoma de México, Apartado Postal 14, Ensenada Baja California, Codigo Postal 22800, México

(Received 29 August 2014; revised manuscript received 10 March 2015; published 30 March 2015)

The initial stages of interface formation for a real-world ferromagnet/antiferromagnet bi-layer system (iron/manganese nitride) are investigated down to the atomic scale using a combination of molecular beam epitaxy, *in situ* scanning tunneling microscopy, and first-principles theoretical calculations. Submonolayer deposition of iron onto manganese nitride nanopyramid surfaces results in an unexpected yet well-ordered structural and magnetic arrangement. It is shown that although the island structures seen in scanning tunneling microscopy images are of single monolayer height, their chemical composition, based on Auger electron spectroscopy, conductance map imaging, and theoretical models, does not consist of iron. It is found theoretically that models that consider iron on the surface of manganese nitride are highly unfavorable. Instead, models with iron atoms incorporated into specific subsurface layers are most stable, in excellent agreement with Auger spectroscopy measurements. Calculations also reveal the magnetic alignment of iron with the manganese nitride layers.

DOI: 10.1103/PhysRevB.91.094433 PACS number(s): 75.30.Et, 68.37.Ef, 71.15.Mb, 75.25.−j

The importance of iron to the field of thin and ultrathin films cannot be overstated, and its relevance to modern spintronic material applications is without question. Being *the* canonical ferromagnetic (FM) material, its properties in various material systems continue to be of very high interest till the present day. For example, many recent studies focused on the growth and properties of Fe on topological insulators, 4*d* transition-metal surfaces, wide-band-gap semiconductors, and carbon-based materials such as C_{60} and graphene [1–6].

Clearly of great importance to any material system is how the Fe grows and couples magnetically to it. This is of fundamental importance to the field of magnetic exchange-bias systems [7,8] which are ubiquitous in modern magnetic recording technology, since the discovery of giant magnetoresistance [9,10]. Ideally, the FM material, coupled directly to an antiferromagnetic (aFM) layer (such as chromium), would form a perfect atomically sharp interface, and the two magnetic layers would couple directly across the interface. Studies have shown that the perfect interface model is unrealistic however, and the complication in the structural arrangement can lead to complex magnetic arrangements as well [11,12].

Exploring the manner in which Fe adapts to different aFM surface environments could lead to new insights into this complex behavior and open new pathways to achieving more successful devices as well as fundamental understandings. In the present study, we choose manganese nitride [$Mn_3N_2(001)$], having a Néel temperature of 652 °C (well below the Curie point of Fe, 770 °C), as the aFM surface. This surface is well studied experimentally, including by spin-polarized scanning tunneling microscopy (SP-STM), detailing its structural, electronic, and magnetic properties. Consisting *in the bulk* of two MnN layers followed by one Mn layer with purely *in-plane* aFM spin directions [13], this structure manifests at the surface a more complex orthogonal, terrace-dependent spin ordering [14]. Such a surface forms an ideal yet challenging testing ground to see the effect of Fe, and as shall be shown, the results are hardly predictable.

Samples are prepared using molecular beam epitaxy (MBE) by first depositing $Mn_3N_2(001)$ films on MgO(001) substrates, for which a detailed growth procedure can be found elsewhere [14,15]. Fe is subsequently deposited at substrate temperatures ranging from RT (room temperature, 25 °C) and up to 200 °C. The Fe coverage ranges between 0.15 and 0.41 monolayers (ML); the samples are not annealed after Fe deposition. The growth is monitored using a 20 keV reflection high energy electron diffraction (RHEED) system. Following preparation, the samples are investigated by RT STM and Auger electron spectroscopy (AES). All STM images are acquired in constant current mode and with an Fe coated tungsten tip. Differential conductance (dI/dV) maps are concurrently acquired in order to identify the electronic and magnetic properties of our samples.

First-principles total energy calculations are performed under the spin-polarized density functional theory as implemented in the plane waves-self-consistent field code of the QUANTUM ESPRESSO package [16]. The generalized gradient approximation adopted in a Perdew-Burke-Ernseroff functional is used to treat the exchange-correlation potential [17]. To expand the valence Khon-Sham states we use a cutoff energy of 30 Ry and Vanderbilt ultra-soft pseudopotentials in order to replace the effect of core electrons [18]. Energetic convergence is achieved when the Hellman-Feynman forces are less than 0.002 Ry/Å. Brillouin zone integration is done

*Corresponding author: smitha2@ohio.edu

 ©2015 American Physical Society

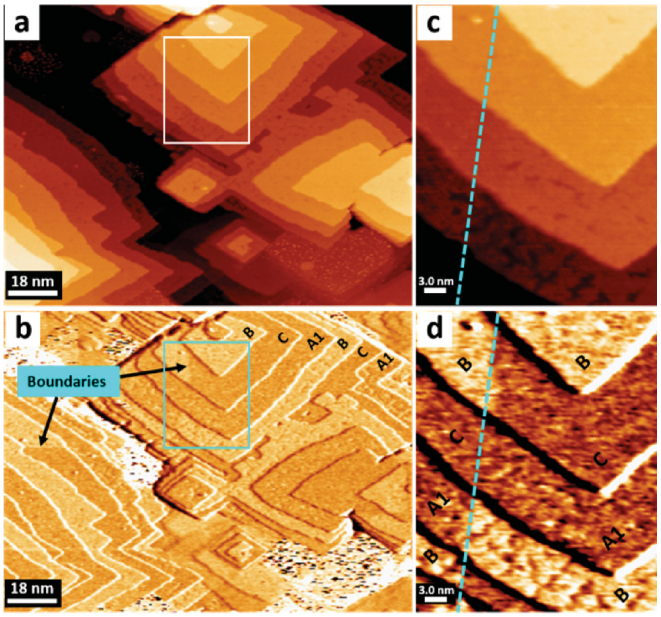

FIG. 1. (Color online) (a) STM topograph and (b) corresponding dI/dV map of the $Mn_3N_2(001)$ substrate ($V_s = -0.3$ V; $I_t = 0.1$ nA). (c) and (d) represent zoom-in views corresponding to the rectangular boxed areas shown in (a) and (b), respectively. For particular terraces, both B and A1/C terminations are present on the same terrace (with boundaries indicated by dashed lines).

using a Monkhorst-Pack smearing of 0.01 Ry and a special $6\times6\times1$ k-points grid [19,20]. First, the bulk of Mn_3N_2 is modeled with a body centered tetragonal structure. After relaxation, an aFM structure is found to be most stable. We also find the lattice parameters to be $a = b = 2.94$ Å and $c = 11.97$ Å, which are in good agreement with previous reports [21]. The Fe adsorption on the surface is analyzed with the surface formation formalism, which is adapted for the Mn_3N_2 system following the work of Qian *et al.* [22].

Presented in Fig. 1 are an STM topograph (a) and corresponding dI/dV map (b) of the $Mn_3N_2(001)$ substrate prior to Fe deposition. The surface consists of atomically smooth square-like terraces separated by single atomic height steps, forming a pyramidal morphology. Using dI/dV mapping, the electronic structure of the nanopyramids is investigated; at small negative sample bias, the sequence *at the surface* consists of one (B) bright terrace (higher dI/dV signal) followed by two (C and A1) darker terraces (lower dI/dV signal), still having a three-layer periodicity. As will be shown, all surface layers are MnN layers, with differences between A1, B, and C coming only in deeper layers. The three-layer sequence at the surface is consistent with previous electronic studies of the $Mn_3N_2(001)$ surface [14].

Zoom-in views of the rectangular boxed regions from Figs. 1(a) and 1(b) are shown in Figs. 1(c) and 1(d). It can be observed in Fig. 1(d) that on a single terrace, both B and A1/C terminations are present, with boundaries indicated by dashed lines. This type of mixed terrace is commonly seen and is due to stacking faults; although within a terrace these interruptions appear, across multiple terraces the expected sequence is preserved [with occasional exceptions; see, e.g., Fig. 3(b)].

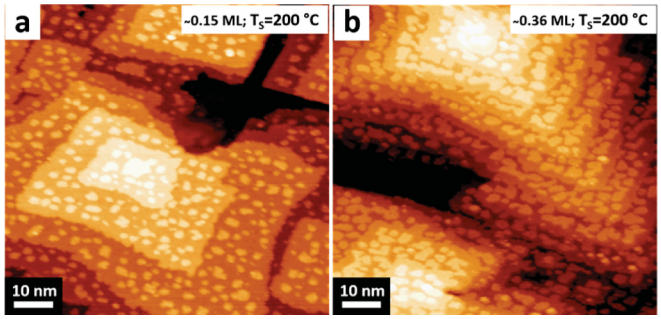

FIG. 2. (Color online) STM topographs for two selected island coverages and corresponding substrate temperatures during growth ($V_s = -0.7$ V; $I_t = 0.1$ nA).

Shown in Fig. 2(a) is a topographical image of a $Mn_3N_2(001)$ nanopyramid surface after depositing ~0.15 ML Fe at a sample temperature of 200 °C (note that the deposition amount quoted is an estimate based on the atomic flux monitor calibration and the STM measured island coverage). Clearly visible are small islands (~1–2 nm in width), having somewhat random shapes, decorating all visible terraces. As shown below [inset to Fig. 3(a)], their heights are only a single atomic layer. It may also be noticed that there is a clear roughening of the step edges as compared to the bare substrate, indicating a possible reaction of the Fe with the substrate. For a higher coverage of ~0.36 ML Fe [Fig. 2(b)], one sees more expanded island shapes as well as even more step edge roughening; sharp terrace corners are no longer visible.

In order to explore island growth space further, additional experiments with the substrate held at 100 °C and at RT were also carried out. The results are qualitatively the same with one small difference being a possible increase in sticking coefficient. For all cases, RHEED patterns showed no change in the lattice constant and no additional phases, implying that the islands are coherent with the substrate.

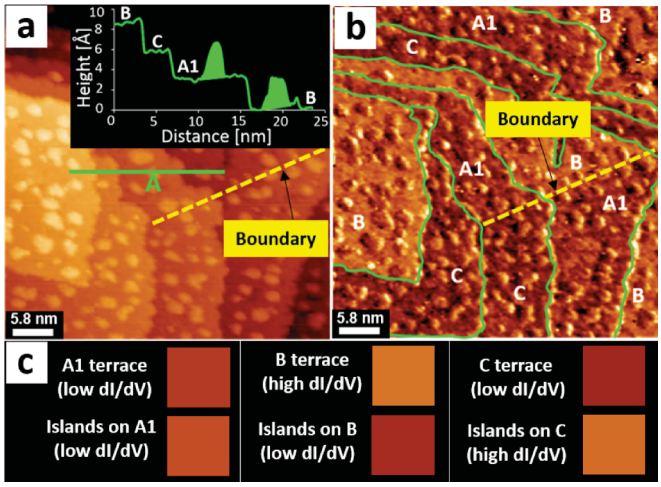

FIG. 3. (Color online) (a) STM topograph and (b) corresponding dI/dV map for the 0.15 ML case ($V_s = -0.3$ V; $I_t = 0.1$ nA). The inset in (a) is a line profile taken along path A. (c) Contrast map from (b) showing the electronic contrast differences between islands and corresponding substrate terraces.

TABLE I. Island coverages, estimated AES Fe:Mn ratios for the cases of Fe islands only and Mn islands only (with Fe in deeper layers) on the surface, and measured Fe:Mn AES ratios.

Island coverage (ML)	Case of Fe islands (%)	Case of Mn islands (%)	Measured (%)
0.15 ± 0.02	6.38 ± 0.32	2.27 ± 0.61	2.16 ± 0.75
0.17 ± 0.01	7.29 ± 0.36	2.50 ± 0.67	2.84 ± 0.44
0.36 ± 0.04	16.82 ± 0.84	5.09 ± 1.40	5.17 ± 0.37
0.41 ± 0.02	19.62 ± 0.98	5.67 ± 1.60	5.71 ± 0.58

Figures 3(a) and 3(b) show an STM topograph and corresponding dI/dV map, respectively, for the 0.15 ML case. The island heights are all about the same (2.28 ± 0.13 Å), as seen in the line profile shown in the inset to Fig. 3(a). Also, the measured step heights and electronic contrasts between adjacent pairs of terraces (A1-B, B-C, and C-A1) are consistent with the surface before Fe deposition (described above) as well as previously published results [14], showing that the terrace electronic properties are unaffected by the islands. One unique feature of this surface region is the presence of a stacking fault boundary within one of the terraces, as indicated by a dashed line; this boundary has to be taken into account when interpreting the dI/dV contrast on the islands from differing terraces presented in Fig. 3(c) (discussed below).

To determine the composition of the observed islands, we performed AES measurements by measuring AES peak intensities obtained from derivative spectra with corrections for Fe and Mn sensitivity factors. Surprisingly, we find Fe:Mn ratios of only a few percent (see Table I).

To know whether or not such values are consistent with Fe atoms at the surface, it is necessary to model the AES Fe:Mn ratios, which requires some models for the stacking sequences of Mn and MnN layers. Therefore, we turn to theoretical calculations. Beginning with just the $Mn_3N_2(001)$ substrate, Fig. 4(a) shows a partial atomic model (with four terraces) of a manganese nitride nanopyramid. Three different models (as indicated within dashed boxes), corresponding to the three unique terraces seen in the STM images, are presented: (1) model A1, consisting of MnN-Mn-MnN-Mn-MnN . . . [an inversion of the expected layer sequence Mn-MnN-MnN-Mn-MnN . . . within the top two layers (model A, not shown)]; (2) model B, consisting of MnN-MnN-Mn-MnN-MnN . . . ; and (3) model C, consisting of MnN-Mn-MnN-MnN-Mn . . . , which has the identical layer sequence as model A1 only within the first three layers.

In terms of surface energy, the presented three models are all lowest energy over a particular range of chemical potential (see Fig. 5). First, and surprisingly, the calculations show that the inverted A1 model is energetically much more favorable than model A over the entire range of chemical potential. Model C becomes more favorable than model A1 at less Mn rich conditions at about 1 eV, and model B becomes most favorable at even less Mn rich conditions at about −0.2 eV.

The AES ratio is then modeled by taking into account the contributions from the islands as consisting only of Fe and the

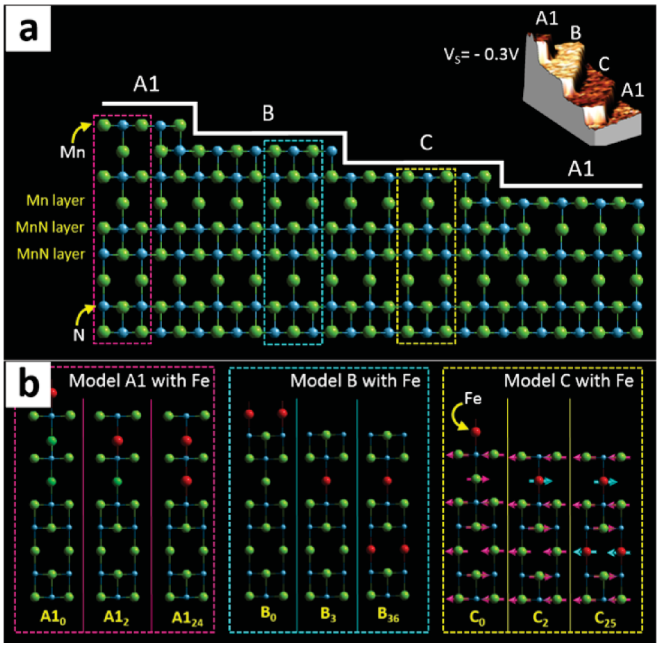

FIG. 4. (Color online) (a) Atomic model of $Mn_3N_2(001)$ nanopyramids in which three different types of terraces can be observed: A1, B, and C; the inset represents a three-dimensional rendered STM image of part of one pyramid to show the correspondence with the actual model. (b) Atomic models for A1, B, and C terraces with Fe atoms (in red) at different locations. In addition, the panel for model C shows the magnetization directions of different layers. Differently colored arrows on the Fe and Mn atoms indicate the different magnetic moments.

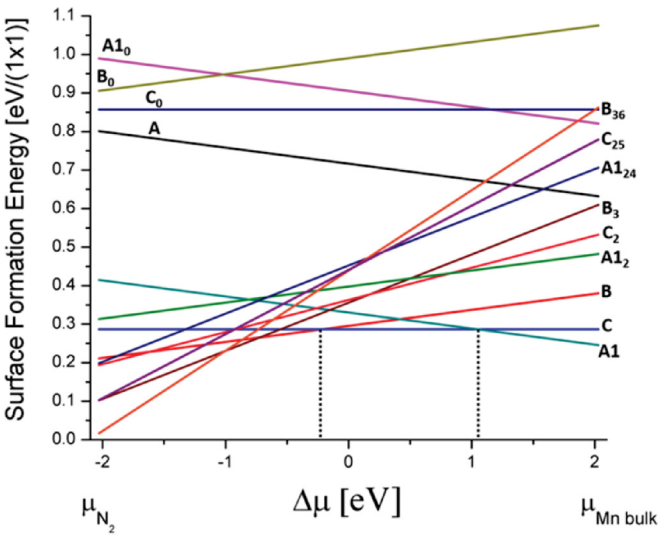

FIG. 5. (Color online) Surface formation energy plots versus chemical potential for the models shown in Fig. 4.

underneath layers being MnN and/or Mn (with their successive contributions to the AES signal exponentially diminishing). Since the AES signal reflects an average of a large area of the surface covering many nanopyramids, we also take an average of the three different possible stacking sequences A1, B, and C, all of which are observed by STM on the same sample. In this manner, for the 0.41 ML coverage case we estimate an Fe:Mn ratio of ∼19.62%, whereas we only measure ∼5.7%. The same trend is obtained for all the coverage cases (see Table I). This disagreement indicates that the islands are not (or not entirely) made of Fe atoms.

Therefore, we consider the possibility that the Fe atoms react somehow with the $Mn_3N_2(001)$ surface, perhaps incorporating into the top few surface layers, which could lead to islands having a different composition. In order to identify possible locations for Fe atoms within the $Mn_3N_2(001)$ structure, Fe is introduced, and Fig. 4(b) shows the A1, B, and C models each with three model variations in which Fe occupies different site locations (including on top and within the $Mn_3N_2(001)$ structure). Each model is denoted via subscripts referring to the layers in which Fe atoms are located. We find that Fe atoms do not occupy Mn sites within MnN layers since this is energetically unfavorable. Instead, Fe atoms are found to favorably occupy Mn sites within the Mn layers, and doing this even results in an overall lowering of the total surface energies at the N-rich side, as can be seen in Fig. 5 where models B_3 and B_{36} become more favorable than model B. Importantly, the results show that it highly unfavorable for Fe atoms to be at the surface as models $A1_0$, B_0, and C_0 are very high in energy. But placing Fe into successive subsurface Mn layers continually lowers the energy, first for models $A1_2$, B_3, and C_2 and then for models $A1_{24}$, B_{36}, and C_{25}. Iron atoms in more than one layer are better than in only one layer.

Naturally, the Fe atom incorporation leads to Mn atom replacement and subsequent removal of Mn from subsurface layers. We therefore propose that the observed islands are formed from the ejected Mn. In order to confirm this picture, we once again carried out AES Fe:Mn ratio simulations, placing Fe atoms into lowest energy configurations ($A1_{24}$, B_{36}, and C_{25}). Taking an average of the simulated ratios based on the three possible configurations results in estimates, for the various Fe depositions, which are in excellent agreement with the measured AES Fe:Mn ratios (see Table I).

Referring back to Figs. 3(b) and 3(c), the electronic contrast of the islands from differing terraces can now be discussed in terms of Mn islands residing on top of $A1_{24}$-,B_{36}-, and C_{25}-structured surfaces. We consistently find not less than three different island contrasts, dependent only on the island's terrace. As shown in Fig. 3(c), we observe dark islands on bright (B) terraces, light islands on dark (C) terraces, and dark islands on dark (A1) terraces. Due to the stacking fault (indicated by the dashed line), which results in a sequence of three low dI/dV (dark) terraces, the middle one contains two types of island contrasts: dark on dark above the A1 region and light on dark above the C region. Although the data was acquired using an Fe-coated W tip, the contrast observed here is purely electronic based on (1) a lack of expected magnetic contrast on the terraces themselves [14], and (2) the fact that an applied *out-of-plane* magnetic field of ∼0.4 T did not result in any changes to the islands dI/dV contrasts.

As further proof of the chemical nature and electronic properties of the islands, we carried out additional experiments, depositing Mn on $Mn_3N_2(001)$ nanopyramids, finding identical dI/dV island contrasts as shown here for the case of Fe deposition. Having established three dI/dV electronic contrasts for the islands, we note that this is exactly consistent with the three-layer periodicity of the $Mn_3N_2(001)$ structure. In fact, the islands' contrasts are consistent with a continuation of the same chemical sequence as for the $Mn_3N_2(001)$ itself. This may indicate that either (1) the electronic properties are determined largely by the Mn atoms, or (2) some islands may contain N, a possibility not entirely unexpected based on the theoretical finding (as well as on the actual growth procedure) that all terraces (first layers) consist of MnN. Atomic rearrangements at the surface could result in N atom exchanges (note that surface N content does not affect the Fe:Mn ratios).

Possible incorporation pathways for Fe atoms are (1) at the step edges (indicative of this is the roughening observed after Fe deposition; see Fig. 3), (2) through direct exchange with surface Mn atoms, and (3) through the defects that are present on the terraces (as also observed in Fig. 1). Since we observe islands on all terraces (including the very top ones) we have to consider possibilities in which the ejected Mn atoms can migrate up and/or down the terrace steps, and maybe even up through the defect sites. Of course this behavior is only speculative, and theoretical calculations would be necessary to clarify these dynamical processes that lead to island formation.

After having determined the locations of the Fe atoms within the $Mn_3N_2(001)$ nanopyramids, theory calculations also find the magnetic moment directions and values for the Fe_{Mn} substitutions. Interestingly, the Fe atoms adopt the same magnetization directions as for the replaced Mn atoms, i.e., Fe atoms couple ferromagnetically with atoms within the same layer [other Fe atoms (Fe-Fe coupling) and/or not yet substituted Mn atoms (Fe-Mn coupling)] and antiferromagnetically with adjacent layers [as depicted in the panel for model C from Fig. 4(b)]. These results are valid for all three models (A1, B, and C). For the specific case of the lowest energy models ($A1_{24}$, B_{36}, and C_{25}), compared to a 0.00 eV/[Fe-Fe(Mn) pair] energy value for Fe-Fe and Fe-Mn FM coupling within the same layer, the aFM coupling is far less favorable, with values ranging from 0.35 to 0.77 eV/(Fe-Fe pair) for Fe-Fe, and 0.32 to 0.72 eV/(Fe-Mn pair) for Fe-Mn. The actual magnetic moment values for the Fe_{Mn} substitutions range from 2.50 to 2.68 μ_B while the Mn atoms in the same sites had magnetic moments ranging from 3.21 to 3.43 μ_B. Certainly, it would be desirable to obtain experimental evidence for the magnetic character of the substituted Mn sites within the sample; future studies using magnetic dichroism are possible but highly nontrivial due to the high Néel point of Mn_3N_2.

In conclusion, we find that the simple deposition of Fe onto $Mn_3N_2(001)$ results in the unexpected substitution of Fe for Mn within Mn layers and the formation of Mn (possibly MnN) islands on top. The islands take on an electronic character consistent with a simple continuation of the normal three-layer chemical periodicity of $Mn_3N_2(001)$. Extending beyond this study to the formation of a possible Fe/$Mn_3N_2(001)$ exchange biased system, such a complex interfacial structure as we find

here would undoubtedly play a very important role in the overall magnetic behavior. It is furthermore very likely that similar behavior to that shown here will occur in other aFM/FM systems, necessitating similar investigations.

This research was supported by the U.S. National Science Foundation under Grant No. DMR-1206636. The authors thank Dr. M. Kordesch for back-coating MgO(001) substrates with titanium and also J. Corbett, S. Pandya, and K. Wang for useful discussions. N.T. thanks DGAPA (Project No. IN103512) and Conacyt (Project No. 164485) for financial support. Calculations were performed in the DGCTIC-UNAM supercomputing center, under Project No. SC15-1-IR-15. WSXM software was used for image processing [23].

[1] I. Vobornik, G. Panaccione, J. Fujii, Z.-H. Zhu, F. Offi, B. R. Salles, F. Borgatti, P. Torelli, J. P. Rueff, D. Ceolin, A. Artioli, M. Unnikrishnan, G. Levy, M. Marangolo, M. Eddrief, D. Krizmancic, H. Ji, A. Damascelli, G. van der Laan, R. G. Edgell, and R. J. Cava, Observation of distinct bulk and surface chemical environments in a topological insulator under magnetic doping, J. Phys. Chem. C **118**, 12333 (2014).

[2] V. Sessi, F. Otte, S. Krotzky, C. Tieg, M. Wasniowska, P. Ferriani, S. Heinze, J. Honolka, and K. Kern, Complex trend of magnetic order in Fe clusters on 4*d* transition-metal surfaces. I. Experimental evidence and Monte Carlo simulations, Phys. Rev. B **89**, 205425 (2014).

[3] S. J. Pearton, C. R. Abernathy, M. E. Overberg, G. T. Thaler, D. P. Norton, N. Theodoropoulou, A. F. Hebard, Y. D. Park, F. Ren, J. Kim, and L. A. Boatner, Wide band gap ferromagnetic semiconductors and oxides, J. Appl. Phys. **93**, 1 (2003).

[4] W. Lin, A.-O. Mandru, A. R. Smith, N. Takeuchi, and H. A. H. Al-Brithen, Iron on GaN(0001) pseudo-$1\times1(1+1/12)$ investigated by scanning tunneling microscopy and first-principles theory, Appl. Phys. Lett. **104**, 171607 (2014).

[5] T. Lan Anh Tran, D. Çakir, P. K. Johnny Wong, A. B. Preobrajenski, G. Brocks, W. G. van der Wiel, and M. P. de Jong, Magnetic properties of bcc-Fe(001)/C_{60} interfaces for organic spintronics, Appl. Mater. Interfaces **5**, 837 (2013).

[6] A. Reserbat-Plantey, P. Gava, N. Bendiab, and A. M. Saitta, First-principles study of an iron-based molecule grafted on graphene, Europhys. Lett. **96**, 57001 (2011).

[7] J. Nogués and I. K. Schuller, Exchange bias, J. Magn. Magn. Mater. **192**, 203 (1999).

[8] R. L. Stamps, Mechanisms for exchange bias, J. Phys. D: Appl. Phys. **33**, R247 (2000).

[9] A. Fert, Nobel lecture: Origin, development, and future of spintronics, Rev. Mod. Phys. **80**, 1517 (2008).

[10] P. A. Grünberg, Exchange anisotropy, interlayer exchange coupling and GMR in research and application, Sensor Actuat. A **91**, 153 (2001).

[11] R. Ravlić, M. Bode, and R. Wiesendanger, Correlation of structural and local electronic and magnetic properties of Fe/Cr(001) studied by spin-polarized scanning tunneling microscopy, J. Phys.: Condens. Matter **15**, S2513 (2003).

[12] Y. J. Choi, I. C. Jeong, J.-Y. Park, S.-J. Kahng, J. Lee, and Y. Kuk, Surface alloy formation of Fe on Cr(100) studied by scanning tunneling microscopy, Phys. Rev. B **59**, 10918 (1999).

[13] G. Kreiner and H. Jacobs, Magnetische Struktur von η-Mn_3N_2, J. Alloy. Compd. **183**, 345 (1992).

[14] K. Wang and A. R. Smith, Three-dimensional spin mapping of antiferromagnetic nanopyramids having spatially alternating surface anisotropy at room temperature, Nano Lett. **12**, 5443 (2012).

[15] H. Yang, H. Al-Brithen, E. Trifan, D. C. Ingram, and A. R. Smith, Crystalline phase and orientation control of manganese nitride grown on MgO(001) by molecular beam epitaxy, J. Appl. Phys. **91**, 1053 (2002).

[16] P. Giannozzi, S. Baroni, N. Bonini, M. Calandra, R. Car, C. Cavazzoni, D. Ceresoli, G. L. Chiarotti, M. Cococcioni, I. Dabo, A. Dal Corso, S. Fabris, G. Fratesi, S. de Gironcoli, R. Gebauer, U. Gerstmann, C. Gougoussis, A. Kokalj, M. Lazzeri, L. Martin-Samos, N. Marzari, F. Mauri, R. Mazzarello, S. Paolini, A. Pasquarello, L. Paulatto, C. Sbraccia, S. Scandolo, G. Sclauzero, A. P. Seitsonen, A. Smogunov, P. Umari, and R. M. Wentzcovitch, QUANTUM ESPRESSO: A modular and open-source software project for quantum simulations of materials, J. Phys.: Condens. Matter. **21** 395502 (2009).

[17] J. P. Perdew, K. Burke, and M. Ernzerhof, Generalized gradient approximation made simple, Phys. Rev. Lett. **77**, 3865 (1996).

[18] David Vanderbilt, Soft self-consistent pseudopotentials in a generalized eigenvalue formalism, Phys. Rev. B **41**, 7892 (1990).

[19] M. Methfessel and A. T. Paxton, High-precision sampling for Brillouin-zone integration in metals, Phys. Rev. B **40**, 3616 (1989).

[20] H. J. Monkhorst and J. D. Pack, Special points for Brillouin-zone integrations, Phys. Rev. B **13**, 5188 (1976).

[21] W. R. L. Lambrecht, M. Prikhodko, and M. S. Miao, Electronic structure and magnetic interactions in MnN and Mn_3N_2, Phys. Rev. B **68**, 174411 (2003).

[22] G.-X. Qian, R. M. Martin, and D. J. Chadi, First-principles study of the atomic reconstructions and energies of Ga- and As-stabilized GaAs(100) surfaces, Phys. Rev. B **38**, 7649 (1988).

[23] I. Horcas, R. Fernandez, J. M. Gomez-Rodriguez, J. Colchero, J. Gomez-Herrero, and A. M. Baro, WSXM: A software for scanning probe microscopy and a tool for nanotechnology, Rev. Sci. Instrum. **78**, 013705 (2007).